



## **Design and pre-test evaluation of a low-pressure compressor test facility for cryogenic hydrogen fuel integration**

Downloaded from: <https://research.chalmers.se>, 2026-06-18 12:11 UTC

Citation for the original published paper (version of record):

Jonsson, I., Xisto, C., Lejon, M. et al (2021). Design and pre-test evaluation of a low-pressure compressor test facility for cryogenic hydrogen fuel integration. Proceedings of the ASME Turbo Expo, 2A-2021. <http://dx.doi.org/10.1115/GT2021-58946>

N.B. When citing this work, cite the original published paper.

GT2021-58946

## DESIGN AND PRE-TEST EVALUATION OF A LOW-PRESSURE COMPRESSOR TEST FACILITY FOR CRYOGENIC HYDROGEN FUEL INTEGRATION

Isak Jonsson<sup>1</sup>, Carlos Xisto<sup>1</sup>, Marcus Lejon<sup>2</sup>, Anders Dahl<sup>1</sup>, Tomas Grönstedt<sup>1</sup>

<sup>1</sup>Chalmers University of Technology, Gothenburg, SE-41296, Sweden

<sup>2</sup>GKN Aerospace Engine Systems, Trollhättan, SE-46181, Sweden

### ABSTRACT

*The use of hydrogen as aviation fuel is again resurfacing with unprecedented vigor. It is well known that hydrogen is a formidable heat sink and the use of heat sinks in the compression system of an aero engine may enable not only preheating of the fuel but also improve the gas turbine cycle itself. One such opportunity arises from extracting heat to the fuel as part of the compression process. This work presents the design process and pre-test evaluation of a low-speed compressor test facility dedicated to aerothermal measurements. The design has been derived from a high-speed transonic compressor developed for a large sized geared turbofan engine. The proposed pre-test evaluation methodology provides a comprehensive and affordable way to estimate facility accuracy by virtually addressing all the experimental procedures, from data acquisition to a final performance map. The evaluation of gathering compressor performance parameters via a gas-path investigation process was achieved while relying on results from numerical simulations. The pre-test evaluation details uncertainties introduced throughout this process with transducers, flow and probe specific errors, traverse discretization, and data normalization. A suitable instrumentation configuration is presented which shows that the performance parameters pressure ratio ( $\Pi$ ) and isentropic efficiency ( $\eta_c$ ) can be determined with uncertainties below 1% for most operating conditions and below 0.5% at design conditions.*

Keywords: pre-test evaluation, uncertainty, low-pressure compressor, intermediate compressor duct, numerical simulations, uncertainty analysis, cryogenic hydrogen

### NOMENCLATURE

$A$	Area
$c_{x_i}$	Normalization coefficient
$\delta$	Independent uncertainty
$\eta_c$	Isentropic Efficiency
$h$	Specific Enthalpy
$K_c$	Contraction discharge coefficient
$Ma$	Mach Number
$\dot{m}_{corr.}$	Corrected mass flow – $\dot{m}\sqrt{T/288.15}/(P/101325)$
$N$	Compressor Speed-line
$\Pi$	Pressure ratio
$\phi$	Flow Coefficient
$p$	Pressure
$q$	Dynamic Pressure
$Re$	Reynolds Number
$R_i$	Total Recovery Coefficient
$\rho$	Density
$s$	Specific Entropy
$T$	Temperature
$\theta$	Load Coefficient
$Tu$	Turbulence Intensity
$V$	Velocity
$\varepsilon$	Function uncertainty
$y_0$	Wall Distance

## ABBREVIATIONS AND SUB- & SUPERSCRIPTS

DR	Degree of reaction
LPC	Low Pressure Compressor
$LH_2$	Liquid hydrogen
IGV	Inlet Guide Vane
HEX	Heat Exchanger
DAQ	Data Acquisition
OGV	Outlet Guide Vane
ICD	Intermediate Compressor Duct
$\bar{\xi}_i$	Area Average: $(\sum_i^N \xi_i A_i) / (\sum_i^N A_i)$
$\bar{\xi}_i V_i \rho_i$	Mass Flow Average: $(\sum_i^N \xi_i A_i V_i \rho_i) / (\sum_i^N A_i V_i \rho_i)$
$\bar{\xi}_i$	Time Average
0	Total Pressure
$\xi_i$	Variable index

## 1 Introduction

Green liquid hydrogen ( $LH_2$ ) is one of very few fuel candidates that could enable carbon-neutral medium- and/or long-range commercial aviation [1] and [2]. From a propulsion unit design perspective, the usage of  $LH_2$  adds complexity due to the need for cryogenic storage and poor volumetric energy density, but also offers many opportunities. The distinct properties of hydrogen compared to Jet-A can potentially be explored to improve engine efficiency, as well as to reduce combustion emissions. The relatively high heat capacity and cryogenic storage temperatures present an opening for possible synergies within the engine heat management system. The amount of cooling capacity available can be utilized at several strategic locations within the engine to improve the core thermal efficiency and component durability.

The development of an  $LH_2$  heat management system for commercial aviation is one of the strategic technology areas covered by the EU-H2020 ENABLEH2 project [3]. Chalmers University of Technology and GKN Aerospace, Sweden, established a partnership to investigate the possible use of existing turbomachinery core components to reject engine core heat to the fuel. To support such an effort, a low-speed, low-pressure compressor facility was commissioned as part of ENABLEH2. The purpose of the facility is to investigate the aerothermal performance of a compressor outlet guide vane (OGV) and downstream interconnecting duct (ICD), and therefore verify its practical use as a point of core heat rejection to the fuel.

To fully utilize the hydrogen as a heat sink in the OGV and ICD, an increased wetted area is likely required [4]. This generally introduces higher pressure losses but can also help to radially guide the flow as in [5]. Aerodynamic experimental investigation of multipurpose aerosurface and more advanced strut and duct geometries is a relatively active field. Walker et al. [6] investigated a combined radial and deswirling concept where the

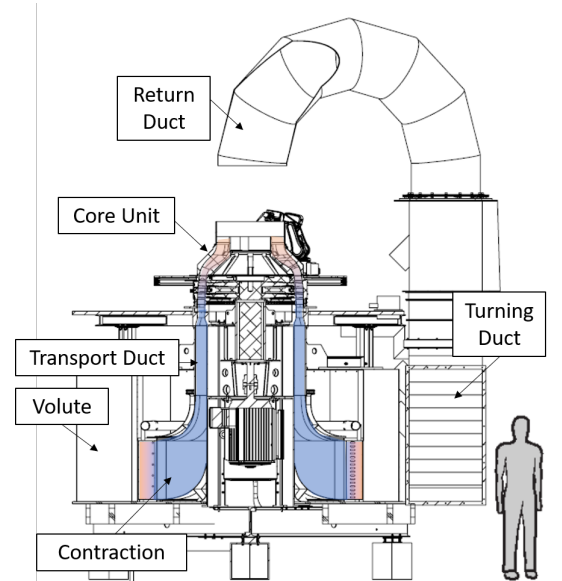


**FIGURE 1.** Schematic view of the low-speed compressor  $LH_2$  heat rejection facility. The facility is part of The Chalmers University of Technology, Laboratory of Fluid and Thermal Sciences. It is designed to achieve an accurate low-speed representation of a state-of-the-art low-pressure compressor designed for a future geared turbofan engine.

OGVs are leaned heavily at Loughborough's University in their low-speed annular test facility. Wallin et al. [7] experimentally investigated a loaded strut in both high and low-speed annular test facilities at Loughborough and the high speed STARCS compressor test facility. The above-mentioned facilities and studies are focused on aerodynamic performance. To achieve high confidence in the planned aerothermal investigation, experimental case verification is required. To the best knowledge of the authors, few experimental investigations of compressor ducts exist in the public domain that provides aerothermal verification results.

In general, fully annular low-speed testing with high aerodynamic and geometric similarities allows for a good compromise between high measurement accuracy and cost, relative to a high-speed counterpart [8]. Even though the Mach numbers are not representative in a low-speed test rig, the importance of such a facility when evaluating compressor performance has repeatedly been shown since many of the numerically challenging flow phenomena are not directly related to compressible effects [8,9]. Moreover, in the interconnecting duct, flow shocks are not expected and therefore a low-speed facility is likely to capture key features providing flow similarity is achieved.

Computational fluid dynamics (CFD) have a large role in supporting modern experimental investigations, both in facility design, pre-test evaluation and post-test investigation [10]. Even though the limitations of CFD in predicting the exact physics

[11], the high availability, low price, and minor random noise make it a suitable aid for several types of experimental studies. This work presents the iterative design process between the aerodynamic designer and the experimentalist to achieve representative flow conditions and the pre-test evaluation by using the results from the performed CFD simulations. The final product is a 2.5—stage, a low-pressure compressor with a tip diameter of 1.2 m, a nominal rotational speed of 1920 RPM, and a nominal power requirement of 147 kW. A schematic of the facility and design parameters are provided in Fig. 1. CFD simulations were performed to evaluate the design at nominal load, part-load, and 5% over-load. In the pre-test evaluation, detailed uncertainty analysis were performed utilizing methods such as Monte Carlo simulations, Taylor Series expansion, existing in-house calibration, and publicly available correlations on a virtual experimental setup based on the numerical flow field. Limitations in the numerical results hinder some aspects of the experimental configuration to be evaluated but the low random noise allows for detailed analysis of individual uncertainty contributions that in experimental conditions are challenging or tedious to isolate. The paper is organized as follows. First, the general application and design challenges of the low-pressure system as relevant to the ENABLEH2 project are described. Subsequently, relevant parts and the findings of the iterative design process and the numerical simulation are presented and discussed. Finally, an uncertainty evaluation of the selected experimental configuration with the aid of the numerical results is presented. This is a critical step before starting the experimental campaign, to allow for final adjustment before manufacturing and curb any faulty assumptions that could lead to non-desired poor experimental data. The same analysis can be performed on existing facilities to estimate the measurement uncertainty.

## 2 Low-pressure compressor design considerations

The design of a compressor is a complex and intricate task. Further complexity is added when designing a low-speed facility as not only is the performance but also flow similarity to the high-speed case is a key design target. In a classical low-speed design task, the success is dependent on several aerodynamic similarities based on Reynolds number, Mach number, Strouhal number, etc. However, for a compressor, parameters like the hub-to-tip ratio, aspect ratio, blade loading, diffusion factor, efficiency, degree of reaction, thickness-to-chord ratio, and solidity are some of the parameters required in order to be able to achieve an accurate representation of the complex flow field. Added to this is the complexity that some high-speed effects cannot be reproduced in a low-speed facility. While the blade loading can be scaled by redesign [8], the effects of shocks cannot be reproduced. Typical compressor design requirements from an aerodynamic perspective include reaching a specified design point in the compressor map in terms of mass flow ( $\dot{m}$ ) and total pressure ratio ( $\Pi$ ) as

well as having a certain stall margin. Depending on the stage location in a multi-stage compressor, high stability may be favored at high- or low-rotational speed in the design phase. The design targets should be achieved with as high efficiency as possible to keep fuel consumption low. The total pressure ratio, efficiency and mass flow are defined in Eq. (1)–(3) with the input variables obtained through experimental and numerical evaluation, further described later in this work.

$$\Pi = (\tilde{p}_{0B})/(\tilde{p}_{0A}) \quad (1)$$

$$\eta_c = 1 - \frac{\tilde{T}_B \Delta s}{\Delta h} = \frac{(\tilde{p}_{0B}/\tilde{p}_{0A})^{(\gamma-1)/\gamma} - 1}{(\tilde{T}_{0B} - \tilde{T}_{0A}) - 1} \quad (2)$$

$$\dot{m} = \rho A \sqrt{\frac{2(p_2 - p_1)}{\rho(1 - (\frac{A_1}{A_2})^2 - K_c)}} \quad (3)$$

The starting point for the present compressor design (hereafter defined as ENABLEH2 compressor) was the two rear stages of the three-stage low-pressure compressor evaluated in [12]. The basic aerodynamic and geometrical similarity was set as the design requirement, constrained by power limitations, maximum RPM, turbulence levels and geometrical constraints. Reynolds number was selected to cover the range from  $3 - 6 \times 10^5$ . In this flow region, the Reynolds effects are relatively predictive [13], and below  $2 \times 10^5$  the risk of laminar separation is considerably higher. Turbulence levels vary substantially in a compressor. The base-level turbulence in the low-speed facility is controlled using turbulence grids [14] and its value ranges from 3-4%. This is expected to mitigate the majority of the low-turbulence behavior, e.g. laminar separation or free-stream turbulent mixing [15]. Nominal power is limited by the cooling power available in the laboratory of approximately 120kW-150kW. The operation pressure in the compressor is close to atmospheric pressure and temperature in the range of 14-21 °C. Non-dimensional compressor specific variables such as flow coefficient  $\phi$  and stage loading  $\psi$  are selected based on the reference compressor design [12]. With the compressor parameters defined, the design of the compressor is iterated between the aerodynamic designer and the experimentalist. The aerodynamic design, from zero-dimensional cycle calculations up to three-dimensional blade stacking and CFD evaluation follows the practice detailed in [16]. In the design effort of the ENABLEH2 compressor, the aerodynamic designer strived to match the performance and geometrical parameters of the reference compressor, while constrained by the

**TABLE 1.** The low pressure compressor system and intermediate compressor duct characteristics and operational conditions at design point.

Low-pressure Compressor	
Rotational Speed	1920 rpm
Mass flow	17 kg/s
Pressure ratio	1.07
Tip Speed	100m/s
Axial Velocity	70m/s
Rotor $Re_c$	$6 \times 10^5$
Avg. Tip radius	620mm
Avg. Hub radius	540mm
Nr. stator Blades (IGV),(s1),(OGV)	75,124,126
Nr. rotor Blades (r1),(r2)	61,69
Avg. Aspect Ratio	2.157
Avg. Tip Clearance	0.75mm
Intermediate Compressor Duct	
$h_i$	0.105
$L$	0.290
$A_i/A_o$	1.0
$\Delta R/L$	0.6

maximum power available to drive the compressor. Another design criterion for the aerodynamic designer was the experimentalist's preference for higher channel height as this leads to lower airspeed, simplification for probe traversing, and thicker blades. The final result concerning the design similitude is shown in Fig. 2, where most target parameters except for Reynolds number differ from the reference design by less than 5%. The pressure ratio is lower as a consequence of the lower rotational speed and matched stage loading  $\psi$ . The compressor general characteristics and typical operational conditions can be seen in Table 1. The compressor blades of the reference compressor had to be re-designed to some degree to make the blades thicker in order to reduce manufacturing cost, enable instrumentation such as pressure taps, and to take differences in flow angles into account.

### 3 Numerical Simulations

The compressor multi-stage performance, including the inlet guide vane (IGV), rotor 1 (r1), stator 1 (s1), rotor 2 (r2), OGV, and ICD, is evaluated numerically using Ansys<sup>TM</sup> CFX 2019 R1, with the RANS  $k - \omega$  SST turbulence model, mixing-plane for the interfaces and enhanced wall functions to approximate the flow in the wall region. The mesh size of a stator and rotor sector is around 200,000 nodes which is based on grid sensitivity study on the reference compressor [16]. Figure 3 shows the mesh distribution for the hub and blade surfaces. Performance variation for constant rotational speed is achieved by varying the inlet stagnation pressure. A turbulence level of 5% is specified at the inlet, and at the outlet, a constant average value of static pressure

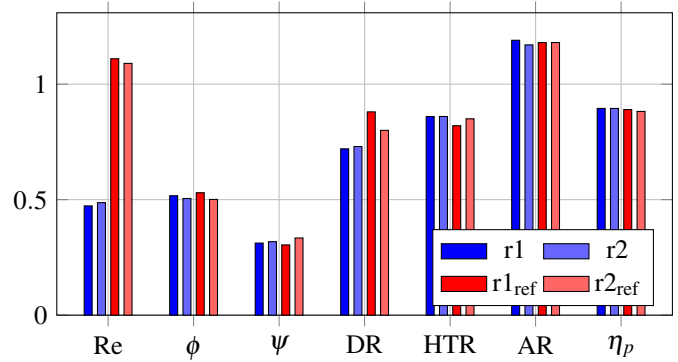


**FIGURE 2.** Facility compressor parameters in comparison to reference engine parameters. AR – Aspect ratio; HTR - Hub-to-tip ratio; DR – Degree of reaction; Re – Chord based Reynolds number;  $\phi$  – Flow coefficient;  $\psi$  – Stage loading;  $\eta_p$  – Polytopic efficiency.

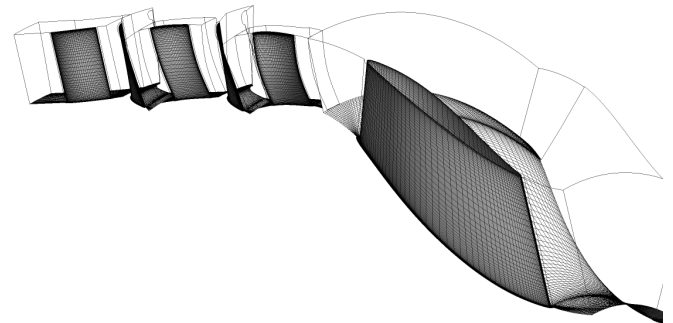


**FIGURE 3.** Mesh distribution of the hub and blade surfaces in the numerical domain.

is imposed. At the design point, the  $y^+$  ranges between 30 and 40 along the different walls. Five different corrected speed lines are evaluated, n0.5, n0.75, n0.85, n1, and n1.05. These characteristics are grouped in the compressor map shown in Fig. 4 as black dashed lines with a marking for each performed simulation. The pressure ratio PR is shown on the y-axis and the corrected mass flow  $\dot{m}_{corr}$  along the x-axis. The isentropic efficiency from the inlet of the IGV to the outlet of the ICD is illustrated by contours and the numerical surge line is shown as a dashed red line. Surge is defined as the point when the stability of the simulations was compromised and no converged steady-state solution was achieved.

### 4 Experimental Configuration

There are several recommended methods in PTC 10 [17] to evaluate the compressor performance, most of which include a combination of static mounted probes, system energy balance of shaft power, or thermal fluxes. The above-mentioned methods allow

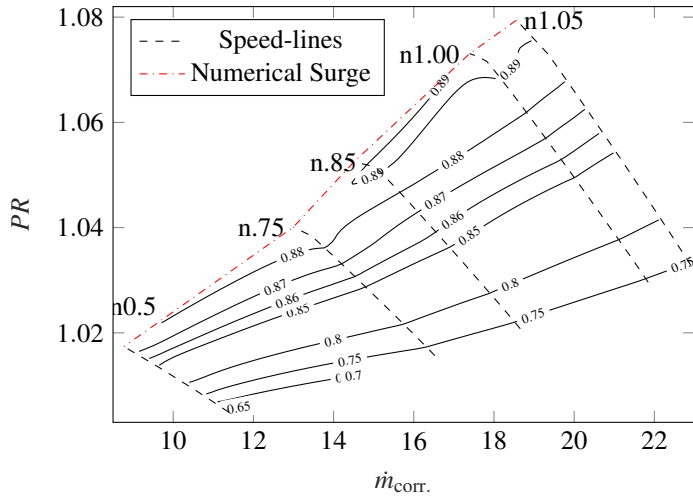


**FIGURE 4.** Compressor performance characteristics based on numerical simulations. The dashed black lines show corrected speed-lines, the dashed red line represents the stall limit, the constant isentropic efficiency areas are defined by the respective contours lines.

for near-instantaneous performance evaluation, but at the cost of limited information and potentially reduced accuracy. The facility does measure the aforementioned as part of the monitoring and operating systems, but the performance of the compressor unit is primarily evaluated using gas-path studies by traversing. Gas path studies by traversing was selected due to the increased level of detail and resolution but come with a higher cost in terms of sampling time and increased complexity when ensuring low uncertainty. The continuous operation of the facility mitigates the majority of the issues related to sampling time. This chapter addresses the second challenge, associated with the intricate and complex uncertainty estimation, and shows that high-quality data are to be expected from this facility. First, the investigated boundaries have to be selected so to allow for the evaluation of the sought quantities. The main target of the facility is to investigate the aerothermal performance of the OGV and ICD, hence priority is placed on the investigation of these boundaries with the highest resolution and access. The same highly detailed boundaries can be utilized to evaluate the compressor performance when complemented with an inlet boundary for the compressor. A lower resolution at the inlet is required due to the relatively low velocity and pressure gradients. Moreover, several intermediate access locations have been added to enable individual stage performance and features within the boundaries.

Gas path studies are based on capturing the gas property changes between two boundaries. These properties are gathered using static or traversing probes as shown in Fig. 5, where the different colors show the type and range of the traverses. The yellow shaded region represents radial traverse access, traverses

colored blue have access from the shroud with a sector of 18 degrees, while the traverses marked with red have full azimuthal access. Upstream the outlet guide vanes, is a small red area that is covered by four radial traverses that access the flow from the hub. The hub can rotate tangentially  $\pm 180^\circ$  to provide full azimuthal access for all four radial traverses. Downstream of the OGV, full azimuthal access is provided by an ABB IBK-1400 with probes gaining access from the outlet of the ICD. The blue dashed lines represent selected measurement boundaries for compressor and ICD performance with  $B_A$  at the IGV inlet,  $B_B$  at the inlet of the OGV, and  $B_C$  at the outlet of the ICD. Figure 5 shows the typical ranges in total pressure and total temperature between the boundaries. At each traverse location, probes can interchangeably be replaced as they all share the same mounting geometry. Using multi-hole probes, Kiel and Prandtl probes, the total pressure ( $p_0$ ), static pressure ( $p$ ), dynamic pressure ( $q$ ), and flow angles are measured. The specific pressure transducer used depends on the configuration, but can be selected as either; PSI-9116, ESP-32HD DTC, FCO432, or FCO-560. The total ( $T_0$ ), and static temperatures ( $T$ ) are gathered using PT100 in different configurations; shielded stagnation temperature probes and standard cylinder probes. Hot-wire anemometry is used to measure instantaneous velocity, turbulence intensity and length scale with a Dantec CTA 56C17 anemometry device and a NI-4461 DAQ. Around the compressor, there are several access holes for radial traverse measurements and pressure taps on the stator blades which are not illustrated in Fig. 5. Optical access is possible along most of the shroud from the trailing edge of the IGV to the outlet of the ICD, except for a short interval above the OGV which is marked by green in Fig. 5. The mass-flow is measured by differential pressure as in the existing low-pressure turbine OGV facility [18], where an FCO-560 is used for differential pressure, temperature and absolute pressure. To mitigate bias errors in the mass-flow measurement, the contraction discharge coefficient is calibrated using an ASME standard venturi meter [19] with an accuracy of 1% at the commissioning of the facility. Denton [20] discuss expensively how entropy and enthalpy derived from measured quantity can be utilized to calculate losses and efficiency in turbomachinery. The pressure ratio and efficiency are primarily evaluated between the boundaries defined by  $B_A$  and  $B_B$ . With gas properties known, thermodynamic relations are used to calculate the isentropic efficiency ( $\eta_{ic}$ ) (Eq. 2).

#### 4.1 Consideration for aerothermal studies

The design of the compressor facility was done without a finalized concept of the ICD-integrated heat exchanger and therefore, the experimental features to be evaluated were estimated and the range for instrumentation prepared. From an experimental point of view, there are two general configurations, one providing open-access to the heat transfer surfaces and another where access is not possible.

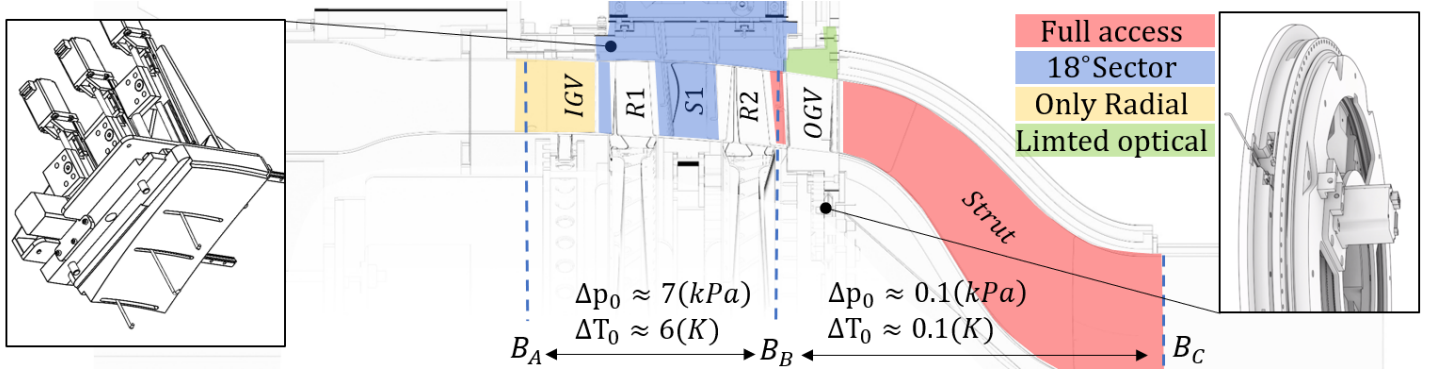


**FIGURE 5.** Schematic view of the compressor with access location, type and expected average measured values. The different colors show the type and range of traverses. The yellow shaded region represents radial traverse access, traverses colored blue can access a sector of 18 degrees while the traverses marked with red have full azimuthal access. The dashed blue lines represent measurement boundaries. The shroud traverse for sector access is shown in the square to the left, and the right shows the hub-mounted full azimuthal traverse system.

The first general configuration includes internal access, which allows for the detailed surface heat transfer to be investigated. This configuration would be similar to the baseline ICD with the possibility of minor modifications, such as mounting fins similar to what was investigated by [21]. The relatively open access, provided by this configuration, allows for smaller and internal detailed surface features to be accessed. Finally, this configuration is suitable for instrumentation based on IR-thermography, which has repeatedly been implemented in Chalmers laboratory of fluid and thermal sciences in similar configurations, e.g. intermediate turbine ducts by [22] and turbine rear structures by [23]. IR-thermography based instrumentation requires internal heating of the investigated surface and solves the conjugate heat transfer problem by measuring the surface temperature. The uncertainty of the method is case dependent, although in [23] it was shown to span from 2%-8% at midspan. This method provides detailed information of surface features such as heat transfer coefficient, and can also be used to locate the transition region [24]. The detailed data can be utilized to verify and calibrate numerical models which are later to be incorporated in the full-scale numerical simulations. The second general configuration is a high solidity heat exchanger where no, or very limited, access is possible. In such a configuration, the effectiveness of the heat exchanger will primarily be evaluated by the energy balance. The instrumentation of such evaluation is relatively simple, requiring the measurement of the temperature difference and mass flow for the two fluids. The challenge for the experimentalist is often to mitigate heat leakage outside the measured boundaries and the relatively high uncertainty in mass flow measurements, material thickness, and material conductivity. The effect of a high solidity heat exchanger on the upstream performance of the compressor can be captured accurately by gas path investigation at boundary  $B_B$ . A range of concepts are currently evaluated at a system level, using the in-house system

performance code GESTPAN [25] and by detailed CFD, similarly as presented in [5].

## 5 Pre-Test Evaluation

This pre-test evaluation aims to evaluate which levels of accuracy are within reach and to make the necessary fine adjustments before manufacturing and the experimental campaign. One key challenge for the experimentalist is to balance the introduced error and mitigate any dominant contributor. The numerical flow field is a powerful tool in this work as it provides a stable virtual environment to benchmark experimental configurations and post processes within. When creating a compressor performance map through gas-path investigation, the experimentalist is required to sample a complex flow field with a discrete number of points over the course of several hours to later reduce it to a single value. In this process, data are undoubtedly lost and errors are introduced. First, in the acquisition, later in the normalization, and finally during the averaging procedure [20]. The performance parameters of a compressor are sensitive to small variations in input variables, especially the isentropic efficiency, where a 0.1% overall input variable uncertainty can produce a 1% measurement uncertainty. To ensure an input variable uncertainty below 0.1%, great caution must be exercised at every step [26]. In the following subsections, the procedures employed in the different steps and associated uncertainties are detailed. Firstly, the acquisition accuracy is evaluated as little is to be achieved if sampled data are noisy or faulty.

### 5.1 Point acquisition accuracy

The accuracy of existing data acquisition systems and transducers is proportional to the measurement range. The measured quality can therefore be greatly increased by arranging sensors

in differential between boundaries, and later referencing all to the single absolute reference. In the present compressor rig, the pressures and temperatures are measured differentially between the illustrated blue-dash boundaries  $B_A - B_B$  or  $B_B - B_C$  in Fig. 5. Sensors at boundary  $B_A$  share a common reference with the ambient absolute pressure and ambient absolute temperature. Furthermore, this method allows for high accuracy measurement in the ICD which would not have been possible in a  $B_A - B_C$  differential configuration because most flow features would have been shadowed in  $B_B - B_C$  by the high enthalpy and entropy added in the compressor (in-between boundaries  $B_A - B_B$ ).

Due to the steady nature of the provided numerical flow-field, no time-dependent statistical errors can be evaluated. The continuous operation of the facility does however allow for a sufficiently long sample time so that statistical errors often can be mitigated below the bias error. Since the contributions from statistical error and bias error often are combined in the square root of the added squared individual contributions, it is reasonable to assume that the bias error will be the larger contributor. From device accreditation or in-house calibration, error  $\delta_{x_i}$  for each measured individual quantity  $x_i$  can be deduced. The dependent variables are evaluated using both Taylor series expansion shown in Eq. (4) as introduced by [27] and Monte Carlo simulations (MCS) shown in Eq. (5) from [28]. The highest uncertainty provided by the two methods was selected. In Eq. (4) and Eq. (5), the function is  $\varepsilon_{\zeta,TS}$  for the Taylor series and  $\varepsilon_{\zeta,MC}$  for the MCS. All transducers are considered to be independent and the total error to be  $\varepsilon_{\zeta}$ . Uncertainties from more intricate measurement methods such as the multi-hole probe were extrapolated from [29] and [30].

$$\varepsilon_{\zeta,TS}(x_1, x_2, \dots, x_n) = \left\{ \sum_{i=1}^n \left( \frac{\partial \zeta}{\partial x_i} \cdot \delta_{x_i} \right)^2 \right\}^{1/2} \quad (4)$$

MCS can for most error estimation be generalized by Eq. (5). Perturbations  $\delta_i$  are introduced on the average value  $x_i$  and the introduced error on the function  $\zeta$  can be estimated as  $\varepsilon_{\zeta}$ . By introducing a significantly large population of perturbations, statistical assumptions can be used to estimate the uncertainty of the function  $\zeta$ .

$$\varepsilon_{\zeta,MC} = \zeta(x_1, x_2, \dots) - \zeta(\tilde{x}_1, \tilde{x}_2, \dots) \quad \tilde{x}_i = x_i + \delta_i \quad (5)$$

For most variables, considerations other than transducer accuracy are necessary in order to accurately capture the true gas properties. Most of these are described in [31]. The authors would like to comment on the pressure and temperature recovery factor  $R_P$  and  $R_T$  as defined in Eq. (6). Often, an uncertainty in

recovery factor above 0.999 is commonly approximated as unity. However, a 0.1% error in the recovery factor in the presented configuration of  $B_A - B_B$  can introduce an uncertainty in the order of the what is introduced from the transducer. The accuracy of the transducers relative to the differential over boundary  $B_A - B_B$  for temperature is  $0.02/6.61 \approx 0.3\%$  and  $\approx 0.1\%$  for the total temperature. Furthermore, the effect from unsteady features and compressible effects can affect the recovery factor. Below is an estimation of identified potential errors and the mitigation from the effects of these.

$$R_i = \frac{x_i}{x_{o,i}} \quad i = T, P \quad (6)$$

The most obvious identified mitigation would be to achieve a recovery factor  $R_i \approx 1$  for the whole operational span as then no compensation or calibration is needed. Most stagnation temperature and pressure probes have a slight reduction from a  $R_T = 1$  in a steady flow of the velocity magnitudes observed in the facility. This static offset in the recovery factor can, to a significant extent, be mitigated by the use of identical probe heads as the measurements are differential. However, the effect of the variations of turbulence and velocity during measurements is still unknown. Instantaneous velocity and turbulence level are measured by hot-wire anemometry, and therefore the effects from turbulence can be compensated following the rationale of [32] and in-house calibration.

Regarding temperature, the authors could not find any documented universal method on how unsteady fluctuation and turbulence should be considered when stagnation temperature is measured. Detailed guidelines on best practice on stagnation temperature measurements are relatively sparse with some guidelines in [26] and in [33], which summarize and expand many details from [34]. However, neither of the aforementioned literature addresses turbulence effects. In [35] the effects from flow unsteadiness are evaluated on a specific temperature Kiel probe. This work shows negligible effects on the temperature recovery factor at a Mach number of 0.3 for all the investigated frequencies. Note that Mach number of 0.3 is the lowest value presented in [35] and this is higher than the highest perceived probe value in the facility.

To compensate for the effect of turbulence on stagnation temperature, we can employ the same rationale used to measure total pressure [32] on total temperature measurement, where the Reynolds decomposition and a reversible process to stagnation state are assumed. Even if this is a gross simplification, at turbulence level of 10% (observed in the NASA low-speed facility compressor facility [36]) would cause an acceptable level of bias error of  $V^2/(2cp)\sqrt{1+3Tu} \approx 0.0037$  K. A completely different approach is to use the static temperature and neglect the dynamic temperature to evaluate the isentropic efficiency was proposed

by [20]. If the dynamic pressure is similar at the two evaluation locations, the effect is proportional to the difference in Mach number. The inlet Mach number is roughly 0.15, whereas in boundary  $B_B$  the maximum Mach number is 0.2. For this operating condition, the dynamic temperature effects are in the order of  $0.009K$ , which is also acceptable. Both stagnation and static temperature will be evaluated in the facility, but for the sake of simplicity, and since any substantial effects on the stagnation temperature recovery coefficient are expected, the stagnation properties are used in all expressions. The multi-hole probe is calibrated for the expected yaw and Mach number following the guidelines in [37]. For pneumatic mean flow measurements in boundary layers, there are corrections for the high velocity and pressure gradients, compressible effects, turbulence effects, and near-wall probe interference which are summarized by Chue in [38]. An experimental investigation in the Superpipe facility by Zagarola et al. [39] used correlations from [38] on a pitot-static probe of 0.9mm operating at probe Reynolds numbers similar to what is expected in this facility with effects below 0.5%. These boundary layer compensations are in general derived from fully developed boundary layers which differ from what can be found in the end-wall boundaries in a compressor. In difference to the pitot-static probe in [39], the 1.6mm diameter kiel probe used in this facility is less sensitive to cone angles, has a smaller displacement, and therefore exhibits smaller effects from the endwalls. Chue recommend with reservation a displacement correlation for kiel probes of  $0.5d$  where  $d$  is the center pipe diameter, [38]. Note that velocity in this area is gathered from hot-wire measurement which follows near-wall corrections from [40]. Even for an ideal probe with no effect from the specific effects of the flow in the boundary layer, errors in the posing of the probe can be a dominant source of uncertainty due to the high gradients. In the current setup, the highest pressure gradient  $\delta p_i / r$  of  $\approx 2000$  can be found in the first sample point at the hub boundary of  $B_B$ . By in-house evaluation, the repeatable resolution of the radial linear actuator is 0.005 mm. By referencing the hub as the datum position, the radial coordinate close to the end-wall could be achieved within 0.01-0.02mm. Note that the absolute coordinate accuracy is much lower due to several real geometry effects and thermal expansion but for the boundary studies, a 0.01-0.02 mm is possible. This allows for a  $\delta r dp_i / dr$  to be in the order of 0.3-0.67% of the measured quantity  $p_i$  at 6000 – 7000 Pa.

Table 2 shows a summary of the expected accuracy for a single point measurement. The mass-flow average differential pressure and temperature between the boundaries  $B_A$ ,  $B_B$  and  $B_C$  are shown. Velocity is shown as the observed velocity at the boundary  $B_B$  or  $B_C$ . The uncertainties  $\delta_i$  are presented as the percentage of the observed mean values between the boundaries.

**TABLE 2.** Values and uncertainties at acquisition of individual traversing points for the evaluated boundaries. Pressures and temperatures are provided as mass-averaged differential value between  $B_A$  and  $B_B$ , whereas velocity is the observed value at boundary  $B_B$  or  $B_C$ .  $BL\delta_i$  are worst case single point uncertainties for boundary layer measurements at boundary  $B_B$

	$p_0$	$p$	$V_{Mag}$	$T$	$T_0$
$B_A - B_B$	7181	5982	69	5.66	6.61
$\delta_i(\%)$	0.12%	0.1%	0.15%	0.02	0.02
$BL\delta_i(\%)$	0.67%	0.68%	0.32%	0.042	0.042
$B_B - B_C$	291.2	817	55.68	0.86	0.002
$\delta_i(\%)$	0.12%	0.1%	0.15%	0.03	0.02

## 5.2 Errors introduced from discretization

The point acquisition accuracy in Table 2 defines the acceptable levels of introduced error from the discretization when traversing. The introduced error from the discretization was evaluated through a mesh sensitivity study on the flow field obtained with CFD. Small adjustments in the axial position of each plane was attractively selected for single point accuracy. The width of the investigated sector was selected to one stator passage, with the wake at midspan placed in the center of the sector. Often, a numerical mesh is refined based on properties such as second derivatives or gradients, but the mesh used to sample data in the facility is kept relatively simple. First, for measuring the wakes, a sufficient number of tangentially uniform distributed points was manually selected so that the mid-span wake could be identified. The mid-span comparison between the selected reduced mesh and the numerical flow field for boundaries with stator wakes can be seen in Fig. 6, where the total pressure and tangential position have been normalized.

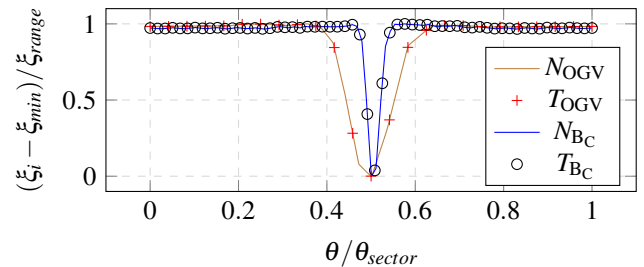


**FIGURE 6.** A comparison between the numerical and selected traverse mesh at mid-span, showing the normalized total pressure of one sector for two boundaries,  $B_C$  and OGV outlet.

The number of radial grid points was iterated using a parabolic function to create a non-uniform distribution that could

capture the low-momentum boundary layer near the endwalls. The quality of the mesh was evaluated by dividing the average of the traversed mean  $p_{0T}$  the numerical mean  $p_{0N}$ , i.e.  $\bar{p}_{0T}/\bar{p}_{0N}$  for area average and  $\bar{p}_{0T}/\bar{p}_{0N}$  for mass-flow average. For boundaries with no stators, such as  $B_B$ , a single tangential profile was required to capture the numerical flow field. The area and the mass-flow weighted average properties were evaluated using cell centered values and are shown for total pressure using different traverse mesh sizes in Fig. 7. The Kiel-probe for total pressure measurement is 1.6 mm in diameter, meaning that the first measurement point is located 0.8 mm above the endwall. The area and mass-flow weighted averaged values were calculated by extrapolation of values below 0.8 mm to the endwall.

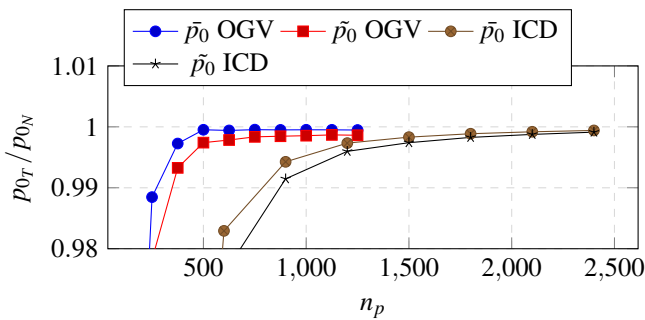
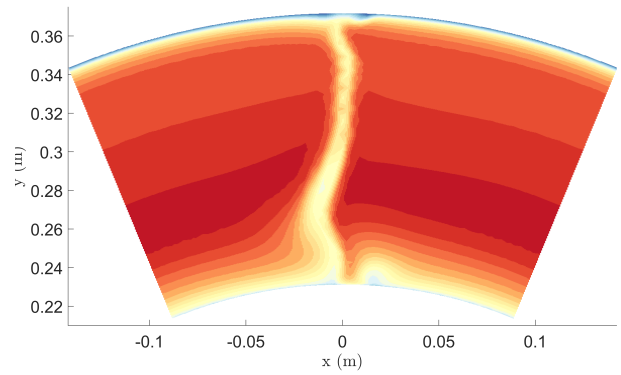


**FIGURE 7.** Results obtained in the grid sensitivity study to determine the required radial point resolution. The results show the variation on the mean dependent on mesh size for interface B and C using both mass-flow and area weighted averages. A mesh is assumed to be sufficiently refined when the discretization error is inferior to 0.2%, which varies substantially for different components.

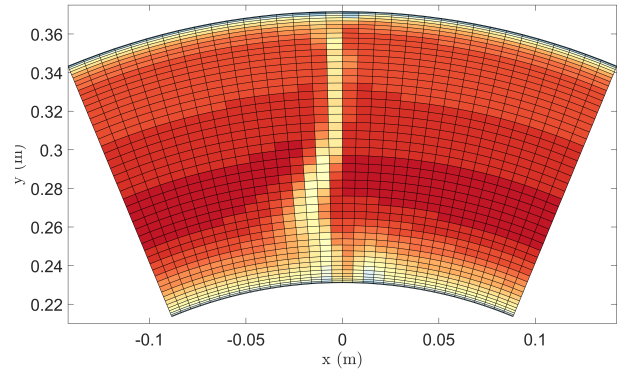
In Fig. 6 and Fig. 8 the high density of points outside the wake might look superfluous, however, it is noted that the mixing-plane circumferential averaging washes out the upstream non-asymmetric features. In the experimental campaign, the flow will contain wake structures from upstream components and the flow field will be much more complex. It is reasonable to assume that a tangential uniform mesh, that accurately captures the most adjacent wake, will capture the more diffused upstream wakes as well. This is not true for a gradient refined mesh.

### 5.3 Data normalization

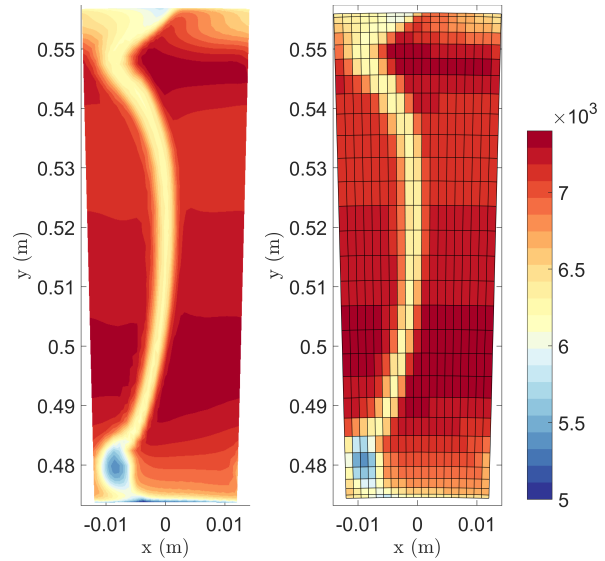
During the operation of the facility, the measurement data requires normalization. Small variations in ambient pressure, temperature, and facility operation will lead to changes in compressor performance. Mass flow and rotational speed are normalized using the classical relations that return corrected mass flow and corrected speed. However, when considering that each averaged data-point is comprised of a data set that is captured during several hours of traversing, further consideration is required. The



(a) Numerical view of boundary  $B_C$



(b) Traversed view of boundary  $B_C$



(c) Numeric view, OGV outlet

(d) Traversed view, OGV outlet

**FIGURE 8.** Total pressure contour plots from the unaltered CFD results (a, c) and the virtually traversed interfaces (b, d) at boundary  $B_C$  (a, b) and at the highest point in the ICD duct traverse plane. The colorscale is valid for all figures

first approach is to scale each traverse value  $x_i(j, t)$  against a fraction of the a time-dependent reference  $x(t)_{ref}$  value and the time average  $\widehat{x_{ref}}$  reference value, throughout the whole data set as shown in Eq.(7). Index  $i$  is the investigated variable,  $j$  the position and  $t$  is time.

$$x_i(j)^* = x_i(j, k) \frac{\widehat{x_i(t)_{ref}}}{x_i(t)_{ref}} \quad (7)$$

Equation (7) provides a relatively simple method that compensates for variations during the operation of the facility, so long as the reference value is a stable and a representative reference. For compressor evaluation with  $B_A$  as inlet, Eq. (7) is sufficient as a single point reference as long as the radial and tangential variations are known. When references inside the compressors are required, e.g. when measuring the properties at the OGV-ICD  $B_B - B_C$ , a single point is often an ill-suited representation of the flow. The high gradients of flow properties together with the flow redistribution with changes in operational conditions make a single representative point hard to find. A typical example of this is when comparing two operational points at the same speed-line. At the first operational point, the reference probe is outside any wake of the upstream stator, and at the second operational point, it is inside the upstream stator wake. The perceived reference total pressure will not represent the actual change of the mean flow total pressure between a change of the two operational points but will include a bias error from the upstream stator wake. One mitigation method is to collect a less sensitive reference value inside the compressor. This can potentially be achieved by using rakes or circumferential end-wall averages as a reference for data normalization, but these cause blockage and may still not suffice due to flow field changes between different operational points.

In this work, another approach is utilized which allows the use of an under-sampled single point reference by scaling it to a more representative reference. The scaling factor  $c_{x_i}$ , as described in Eq. (8) is the factor between the single point reference  $x_i(t)_{ref}$  and the more representative flow average. In Sec. 5.2, the inlet average  $\overline{x_i(j, t)}$  has been shown to produce a sufficiently accurate representation of the flow average properties and can therefore be used as a scaling reference. The scaling is performed by the fraction between the reference and the traversed point value  $x_i(j, k)$ . Since the OGV inlet plane is required to be traversed for OGV performance evaluation, there is no penalty in operational duration for this data normalization.

$$c_{x_i} = \frac{x_i(j, t)}{x_i(t)_{ref}} \quad (8)$$

Later, in the post-processing, the area-averaged scaling factor  $c_{x_i}$  is multiplied by  $\widehat{x_{i,ref}}$  in Eq. (7) before the  $x_i(j)^*$  is calculated.

Note that this process assumes a stable bias offset of the reference probe values during the full plane sampling. Hence, before sampling, the probe must be ensured to be in a relatively stable location and not in a separated flow or other high gradient areas.

#### 5.4 Expected Accuracy

The expected accuracy of any individual measurement is evaluated by combining the single point uncertainty  $\delta_i$  with the discretization uncertainty  $\delta_D$  using Eq. (9). The uncertainties of performance evaluation parameters are evaluated by replacing all measured individual variables  $x_i$  with the expression for the normalize variable  $x_i^*$  in Eq. (4) and Eq. (5).

$$\varepsilon_\zeta = \varepsilon_\zeta(x_1^*, x_2^*, \dots, x_n^*) \quad \delta_i = \sqrt{\delta_{DAQ}^2 + \delta_D^2} \quad (9)$$

The uncertainties of performing this operation on Eq. (1), (2) and (3) are shown in Fig. (9). The proportional contribution from the individual sources is shown as blue for discretization, orange for normalization, and grey for single point accuracy. The total expected error is shown in red. The error in terms of pressure rise is shown in Fig. 9 instead of the total coefficient to improve visibility. The accuracy of mass flow calibration has a potential bias error of 1% which had a dominant effect on the total error calculation. The sensitivity of the mass-flow measurement is an order of magnitude higher. Isotropic efficiency has an uncertainty of 0.5% at the peak pressure range, where the dominant uncertainty contribution arises from temperature measurements. At higher mass-flow and lower pressure ratio, the uncertainties in pressure ratio and efficiency increase while the uncertainty in mass flow remains close to constant.

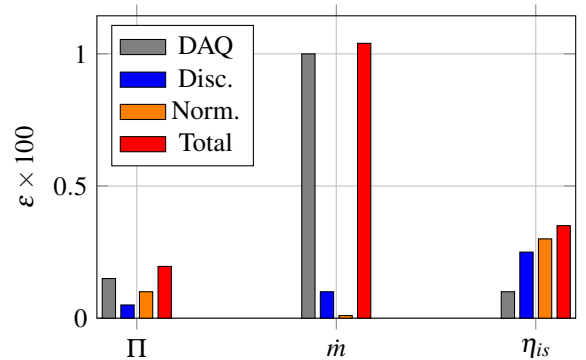


**FIGURE 9.** Bar diagram showing the total uncertainties (red) for compressor evaluation parameters at speed line n.1,  $\dot{m}_{corr} = 17.8$ . The individual contributions from discretization, normalization and single point acquisition are shown as blue, orange and grey respectively.

## 6 Conclusion

This work presents the design considerations and pre-test evaluation of a large-scale, low-speed, low-pressure compressor test facility design for accurate aerothermal studies. The design is based on a high-speed reference engine where key geometrical and aerodynamic flow similarities are achieved. Numerical steady-state RANS simulations have been used to evaluate the final compressor design and to represent the compressor performance over a wide range of operational conditions. The compressor performs as expected, providing a wide range of high-efficiency operations with a good stability margin. The performance of the compressor is primarily to be experimentally evaluated using gas-path studies by traversing selected boundaries. The capability and challenges with such an investigation have been addressed by a pre-test evaluation with the support of the numerical results. Each sampled quantity has been evaluated as if instrumented in the facility, and the effects from uncertainties of data acquisition, flow field turbulence and velocity have been accounted for when calculating the single point accuracy. Furthermore, uncertainties from discretization have been evaluated to select the grid density to sample an area and mass-flow weighted average within a 0.2% of flow average. The results indicate that 2000 points are needed for the ICD outlet and 750 points are required to resolve the flow in the OGV outlet. Finally, the total expected uncertainty is summarized and is evaluated based on the full expression of key performance parameters, including the operational data normalization using both Taylor Expansions and Monte Carlo Simulations. The results from this show that the highest expected uncertainty is given by the corrected mass-flow, with the main contributor coming from the discharge coefficient of the contraction. The total pressure ratio can be captured with an uncertainty below 1% for all pressure ranges, and near the design point, the level of uncertainty is close to 0.2%. The uncertainty of the isentropic efficiency at the same operating point is found to be 0.5%. Important quantification of design choices in the late design phase of an advance aerothermal test facility has been presented. The virtual pre-test evaluation have aided in mitigated many time consuming and expensive post manufacturing modifications otherwise required if experimental data was to be used. Most methods and processes can be utilized in similar facilities especially when complemented with verified numerical results as it allows for isolation of uncertainty sources that is challenging to perform on experimental data, such as discretization errors. The facility presented in this work will primarily perform investigations of modified compressor vane components (ICD and OGV) and to establish their aerothermal performance as possible heat rejection surfaces to the fuel. The results of this will be utilized to calibrate a in-house system level gas-turbine performance code which is currently being adopted for cryogenically LH<sub>2</sub> fueled aircraft in the ongoing ENABELH2 to allow for higher efficiency commercial aviation hydrogen turbofan engines.

## ACKNOWLEDGMENT

The E.U. financially supports this work under the “ENABLEH2 – Enabling cryogenic hydrogen-based CO<sub>2</sub> free air transport” Project co-funded by the European Commission within the Horizon 2020 Programme (2014-2020) under Grant Agreement no. 769241. The authors also acknowledge the support provided by the department of Mechanics and Maritime Sciences at Chalmers University of Technology.

## REFERENCES

- [1] Rompokos, P., Rolt, A., Nalianda, D., Isikveren, A., Senné, C., Grönstedt, T., and Abedi, H., 2020. “Synergistic technology combinations for future commercial aircraft using liquid hydrogen”. Vol. Volume 1: Turbomachinery of *Turbo Expo: Power for Land, Sea, and Air*.
- [2] ISBN 978-92-9246-342-7, 2020. Hydrogen-powered aviation a fact-based study of hydrogen technology, economics, and climate impact by 2050. Report, McKinsey & Company for the Clean Sky 2 JU and Fuel Cells and Hydrogen 2 JU, Belgium, May.
- [3] CORDIS, 2018. *ENABLING cryogenic Hydrogen based CO<sub>2</sub> free air transport (ENABLEH2)*. European Commission CORDIS 769241. European Commission.
- [4] Xisto, C., Abedi, H., Jonsson, I., and Grönstedt, T., 2020. “Development of fuel and heat management systems for liquid hydrogen powered aircraft”. 10th EASN International Conference on Innovation in Aviation and Space to the Satisfaction of the European Citizens.
- [5] Jonsson, I., Xisto, C., Abedi, H., Grönstedt, T., and Lejon, M., 2020. “Feasibility Study of a Radical Vane-Integrated Heat Exchanger for Turbofan Engine Applications”. *Turbo Expo: Power for Land, Sea, and Air*.
- [6] Walker, A., Barker, A., Carrotte, J., Bolger, J., and Green, M., 2013. “Integrated outlet guide vane design for an aggressive s-shaped compressor transition duct”. *Journal of Turbomachinery*, **135**(1).
- [7] Wallin, F., Olsson, J., Johansson, P. P., Krüger, E., and Olausson, M., 2013. “High speed testing and numerical validation of an aggressive intermediate compressor duct”. In *Turbo Expo: Power for Land, Sea, and Air*, Vol. 55232, American Society of Mechanical Engineers, p. V06BT38A003.
- [8] Wisler, D. C., 1985. “Loss Reduction in Axial-Flow Compressors Through Low-Speed Model Testing”. *Journal of Engineering for Gas Turbines and Power*, **107**(2), 04, pp. 354–363.
- [9] Wasserbauer, C., 1995. *NASA Low-speed Axial Compressor for Fundamental Research*. NASA technical memorandum. NASA.
- [10] Drozda, T. G., Axhdahl, E. L., and Cabell, K. F., 2014. “Pre-test cfd for the design and execution of the enhanced injec-

- tion and mixing project at nasa langley research center”. In JANNAF 46th CS/34th APS/34th EPSS/28th PSHS Joint Subcommittee Meeting, Albuquerque, NM (Dec. 2014).
- [11] Denton, J. D., 2010. “Some Limitations of Turbomachinery CFD”. Vol. Volume 7: Turbomachinery, Parts A, B, and C of *Turbo Expo: Power for Land, Sea, and Air*, pp. 735–745.
- [12] Lejon, M., 2018. “Aerodynamic design framework for low-pressure compression systems”. phd Thesis, Chalmers University of Technology, Gothenburg.
- [13] Schaffler, A., 1980. “Experimental and analytical investigation of the effects of reynolds number and blade surface roughness on multistage axial flow compressors”. *Journal of Engineering for Power*, **102**(1), 01, pp. 5–12.
- [14] Roach, P. E., 1987. “The generation of nearly isotropic turbulence by means of grids”. *International journal of heat and fluid flow*, **8**(2), pp. 82–92.
- [15] Mayle, R. E., 1991. “The 1991 IGTI Scholar Lecture: The Role of Laminar-Turbulent Transition in Gas Turbine Engines”. *Journal of Turbomachinery*, **113**(4), 10, pp. 509–536.
- [16] Lejon, M., Grönstedt, T., Glodic, N., Petrie-Repar, P., Genrup, M., and Mann, A., 2017. “Multidisciplinary design of a three stage high speed booster”. In *Turbo Expo: Power for Land, Sea, and Air*, Vol. 50794, ASME, p. V02BT41A037.
- [17] American Society of Mechanical Engineers (ASME), 1997. Performance Test Code on Compressors and Exhausters PTC 10 - 1997(R2014). Standard, ASME.
- [18] Rojo, B., 2017. “Aerothermal Experimental Investigation of LPT-OGVs”. PhD Thesis, Chalmers University of Technology, Gothenburg.
- [19] ASME International, A., 2004. Flow measurement ptc 19.5. Tech. rep., ASME International ASME.
- [20] Denton, J. D., 1993. “The 1993 IGTI Scholar Lecture: Loss Mechanisms in Turbomachines”. *Journal of Turbomachinery*, **115**(4), 10, pp. 621–656.
- [21] Villafañe, L., and Paniagua, G., 2018. “Aerodynamic impact of finned heat exchangers on transonic flows”. *Experimental Thermal and Fluid Science*, **97**, Oct., pp. 223–236.
- [22] Arroyo Osso, C., Gunnar Johansson, T., and Wallin, F., 2012. “Experimental Heat Transfer Investigation of an Aggressive Intermediate Turbine Duct”. *Journal of Turbomachinery*, **134**(5), 05, 051026.
- [23] Jonsson, I., Chernoray, V., and Dhanasegaran, R., 2020. “Infrared thermography investigation of heat transfer on outlet guide vanes in a turbine rear structure”. *International Journal of Turbomachinery, Propulsion and Power*, **5**(3), p. 23.
- [24] Jonsson, I., Deshpande, S., Chernoray, V., Thulin, O., and Larsson, J., 2018. “Experimental and numerical study of laminar-turbulent transition on a low-pressure turbine outlet guide vane”. In *Proc. of ASME Turbo Expo 2020*.
- [25] Grönstedt, T., 2000. “Development of Methods for Analysis and Optimization of Complex Jet Engine Systems”. PhD Thesis, Chalmers University of Technology, Gothenburg.
- [26] Bonham, C., Thorpe, S. J., Erlund, M. N., and Stevenson, R. J., 2017. “Combination probes for stagnation pressure and temperature measurements in gas turbine engines”. *Measurement Science and Technology*, **29**(1), dec.
- [27] Ku, H., 1966. “Notes on the use of propagation of error formulas”. *Journal of Research of the National Bureau of Standards*, **70C**(4), p. 263.
- [28] Rubinstein, R. Y., and Kroese, D. P., 2017. *Simulation and the Monte Carlo method*. Wiley series in probability and statistics. John Wiley & Sons.
- [29] Jonsson, I., Valery, C., and Rojo, B., 2018. “Surface roughness impact on secondary flow and losses in a turbine exhaust casing”. In *Proc. of ASME Turbo Expo 2018*.
- [30] Jonsson, I., 2020. “Experimental aerothermal study on internal jet engine structures”. PhD thesis, Chalmers University of Technology.
- [31] Tropea, C., Yarin, A., and Foss, J., 2007. *Springer Handbook of Experimental Fluid Mechanics*. Springer Handbook of Experimental Fluid Mechanics. Springer.
- [32] Goldstein, S., 1936. “A note on the measurement of total head and static pressure in a turbulent stream”. *Proceedings of the Royal Society of London. Series A-Mathematical and Physical Sciences*, **155**(886), pp. 570–575.
- [33] Zeisberger, A., 2007. “Total temperature probes for turbine and combustor applications”. In *International Symposium on Air Breathing Engines*, Beijing, China, Sept, pp. 2–7.
- [34] Saravanamuttoo, H., 1990. Recommended practices for measurement of gas path. Tech. rep., AGARD, Chigwell-Lane, Loughton, Essex, June.
- [35] Bonham, C., Brend, M., Spencer, A., Tanimizu, K., and Wise, D., 2018. “Impact of Flow Unsteadiness on Steady-State Gas-Path Stagnation Temperature Measurements”. *Journal of Engineering for Gas Turbines and Power*, **140**(12), 08, 122602.
- [36] Camp, T. R., and Shin, H.-W., 1994. “Turbulence Intensity and Length Scale Measurements in Multistage Compressors”. Vol. Volume 1: Turbomachinery of *Turbo Expo: Power for Land, Sea, and Air*.
- [37] Johansen, E. S., Rediniotis, O. K., and Jones, G., 2000. “The Compressible Calibration of Miniature Multi-Hole Probes”. *Journal of Fluids Engineering*, **123**(1), 09, pp. 128–138.
- [38] Chue, S., 1975. “Pressure probes for fluid measurement”. *Progress in aerospace sciences*, **16**(2), pp. 147–223.
- [39] Zagarola, M. V., and Smits, A. J., 1998. “Mean-flow scaling of turbulent pipe flow”. *Journal of Fluid Mechanics*, **373**, p. 33–79.
- [40] Durst, F., and Zanoun, E., 2002. “Experimental investigation of near-wall effects on hot-wire measurements”. *Experiments in Fluids*, **33**(1), pp. 210–218.